IOP Publishing Phys. Med. Biol. 65 (2020) 085012 https://doi.org/10.1088/1361-6560/ab7971

Physics in Medicine & Biology

IPEM Institute of Physics and Engineering in Medicine

OPEN ACCESS

RECEIVED
27 September 2019

REVISED
31 January 2020

ACCEPTED FOR PUBLICATION
24 February 2020

PUBLISHED
20 April 2020

PAPER

Feasibility and limitations of quantitative SPECT for ^{223}Ra

Johan Gustafsson[1], **Emilia Rodeño**[2] **and Pablo Mínguez**[3,4]

[1] Medical Radiation Physics, Clinical Sciences Lund, Lund University, Lund, Sweden
[2] Department of Nuclear Medicine, Gurutzeta/Cruces University Hospital/Biocruces Health Research Institute, Barakaldo, Spain
[3] Department of Medical Physics and Radiation Protection, Gurutzeta/Cruces University Hospital/Biocruces Health Research Institute, Barakaldo, Spain
[4] Faculty of Engineering, Department of Applied Physics I, UPV/EHU, Bilbao, Spain

E-mail: johan_ruben.gustafsson@med.lu.se

Keywords: radium-223, SPECT, activity quantification, quantitative SPECT, Monte Carlo simulation

Abstract

The aim of this paper is to investigate the feasibility and limitations of activity-concentration estimation for ^{223}Ra using SPECT. Phantom measurements are performed using spheres (volumes 5.5 mL to 26.4 mL, concentrations 1.6 kBq mL^{-1} to 4.5 kBq mL^{-1}). Furthermore, SPECT projections are simulated using the SIMIND Monte Carlo program for two geometries, one similar to the physical phantom and the other being an anthropomorphic phantom with added lesions (volumes 34 mL to 100 mL, concentrations 0.5 kBq mL^{-1} to 4 kBq mL^{-1}). Medium-energy and high-energy collimators, 60 projections with 55 s per projection and a 20% energy window at 82 keV are employed. For the Monte Carlo simulated images, Poisson-distributed noise is added in ten noise realizations. Reconstruction is performed (OS-EM, 40 iterations, 6 subsets) employing compensation for attenuation, scatter, and collimator-detector response. The estimated concentrations in the anthropomorphic phantom are also corrected using recovery coefficients. Errors for the largest sphere in the physical phantom range from −25% to −34% for the medium-energy collimator and larger deviations for smaller spheres. Corresponding results for the high-energy collimator are −15% to −31%. The corresponding Monte Carlo simulations show standard deviations of a few percentage points. For the anthropomorphic phantom, before application of recovery coefficients the bias ranges from −16% to −46% (medium-energy collimator) and −10% to −28% (high-energy collimator), with standard deviations of 2% to 14% and 1% to 16%. After the application of recovery coefficients, the biases range from −3% to −35% (medium energy collimator) and from 0% to −18%. The errors decrease with increasing concentrations. Activity-concentration estimation of ^{223}Ra with SPECT is feasible, but problems with repeatability need to be further studied.

1. Introduction

Radionuclide therapy (RNT) with ^{223}Ra dichloride (Xofigo®, Bayer HealthCare) is a treatment option for skeletal metastases in castration-resistant prostate cancer (Parker *et al* 2013). However, the understanding of the mechanisms behind the therapeutic effects is still incomplete (Rubini *et al* 2014, Flux 2017). Hence, methods for quantifying ^{223}Ra activity *in vivo* are potentially valuable to map the distribution of the radiopharmaceutical as a function of time in patients and determine the absorbed doses to lesions and organs.

In addition to the alpha particles responsible for the therapeutic effect, photons are also emitted in the ^{223}Ra decay chain and can be used for gamma-camera imaging. Most commonly, a series of characteristic x-ray photons around 80 keV are used for planar imaging and the activity is estimated under the assumption of equilibrium between ^{223}Ra and its daughters (Carrasquillo *et al* 2013, Chittenden *et al* 2015, Pacilio *et al* 2016*b*, Pacilio *et al* 2016*a*, Murray *et al* 2017). However, there are photons emitted with energies up to more than 1 MeV, with emissions with major yields starting at 832 keV with an abundance of approximately 3%.

Other peaks apart from the characteristic x-rays potentially suitable for imaging are for example at 154 keV, 269 keV and 271 keV, 324 keV, and 402 keV. Details about the gamma spectrum for ^{223}Ra in equilibrium with its daughters can be found in Pibida *et al* (2015), Kossert *et al* (2015) and Collins *et al* (2015).

In general, single photon emission computed tomography (SPECT) is considered to be superior to planar imaging for activity quantification (Dewaraja *et al* 2012). The advantage of SPECT is that the activity distribution is resolved in three dimensions, thereby avoiding the overlap of activity in the anterior-posterior direction inherent to planar techniques. Unfortunately, the combination of a complex photon emission spectrum and the very low activities administered to patients (typically 55 kBq kg^{-1}) makes SPECT imaging of ^{223}Ra challenging because of the low signal-to-noise ratio (SNR) and the need to compensate for the scatter and penetration that constitute a substantial part of the acquired signal.

Owaki *et al* (2017) reported on the possibility of using SPECT for visualization of ^{223}Ra uptake and semi-quantitative tasks, demonstrating the feasibility of tomographic imaging of the radionuclide. Studies of quantitative SPECT have been made by Yue *et al* (2016) and Benabdallah *et al* (2019). Benabdallah *et al* (2019) studied the optimization of SPECT imaging parameters for the radionuclide through a series of phantom measurements, and Yue *et al* (2016) evaluated SPECT reconstruction of a phantom measurement of a sphere 3.5 cm in diameter. The problem of SPECT for ^{223}Ra has also attracted interest in the context of ^{227}Th, where ^{223}Ra is a daughter product that needs to be considered for an accurate quantification (Ghaly *et al* 2019). Still, there is a need to further characterize the properties of SPECT-based activity quantification for ^{223}Ra to allow for its use in patient studies, and in the long term, acquire reliable information about the accumulation of ^{223}Ra in lesions. In particular, we believe that there is a further need for studying the repeatability (i.e. the dispersion caused by noise in the acquired projections) and the behaviour of the estimated activity concentration at the very low concentrations that might be expected to occur in clinical practice.

This study aims to investigate the feasibility and limitations of quantitative SPECT for ^{223}Ra by a series of phantom measurements and Monte Carlo simulations in various geometries. The main focus is the estimation of activity concentration in lesions. The long-term goal is to characterize the properties to allow for SPECT-based future studies in patients and to identify the limiting factors for accurate image-based quantification for this radionuclide.

2. Materials and methods

2.1. Phantom measurements

A solution of ^{223}Ra with an activity concentration of 4.6 kBq mL^{-1} was prepared and used to fill three spheres with volumes 5.5 mL (sphere 1), 11.5 mL (sphere 2), and 26.4 mL (sphere 3). The phantom used was an IEC phantom filled with 10 L of water. Three different source geometries were considered: only the largest sphere in the phantom in a cold background, all three spheres mounted in the phantom in a cold background, and all three spheres in the phantom with a sphere-to-background ratio (SBR) of 20:1. Because it was believed to be important to acquire images for different activity concentrations in the spheres, the phantom was prepared and imaged at different time points after preparation. Hence, not all geometries could be considered for all activity concentrations. The combinations of source geometries and activity concentrations that were considered are specified in table 1.

Projections were acquired with a GE Infinia Hawkeye SPECT/CT (GE, Fairfield, CT, USA) in 60 projections over 360° in 128 × 128 matrices with a pixel size of 4.4 × 4.4 mm^2 and an acquisition time of 55 s per projection. Either a medium-energy general-purpose (MEGP) or high-energy general-purpose (HEGP) collimator was used. The energy window was 20% centred at 82 keV.

2.1.1. Reconstruction

Tomographic images were reconstructed using Ordered Subsets Expectation Maximization (OS-EM) with 40 iterations and 10 angles per subset (i.e. 6 subsets) employing compensation for attenuation, scatter using the Effective Source Scatter Estimation (ESSE) method (Frey and Tsui 1996), and collimator-detector response including penetration, scattering in the camera head, and characteristic x-rays from the collimator, derived from Monte Carlo simulations of point sources in air at different distances from the collimator (He *et al* 2005, Frey and Tsui 2005). The geometry used for the attenuation and the model-based scatter compensation was based on the CT image that was converted to densities using a two-linear segment function determined from measurements in a phantom with insert with known densities.

The SPECT images (in units of 'counts' per second per voxel) were scaled to activity per voxel by division with the system sensitivity measured in air with a thin layer of activity in a Petri dish at a distance of 10 cm from the collimator. The whole field-of-view was used for the determination of sensitivity. One problem with this calibration approach is that the reconstruction program normalizes the images to scatter- and

Table 1. SPECT acquisitions performed for the sphere phantom.

Spheres	Activity concentration/(kBq mL^{-1})	SBR
MEGP collimator		
3	4.5	1:0
1, 2, 3	4.5	1:0
1, 2, 3	3.4	20:1
1, 2, 3	2.5	20:1
1, 2, 3	1.6	20:1
HEGP collimator		
1, 2, 3	4.5	1:0
3	3.6	1:0
1, 2, 3	3.4	20:1
1, 2, 3	2.5	20:1
1, 2, 3	1.6	20:1

penetration-free conditions. While it was assumed that the in-air measurement gives a valid calibration factor with respect to the condition of not being affected by scatter from the phantom, an assumption of penetration-free conditions would not be valid. In order to correct for this, the sensitivity was normalized to the total-to-geometric ratio at 10 cm for the collimator-detector kernels used in the reconstruction. The number of counts in the measured projection was also corrected for general background by acquiring a blank projection, i.e. a projection with no source in the camera.

2.1.2. Evaluation

The SPECT images were interpolated to the same voxel size as the CT image using linear interpolation to facilitate the evaluation. Volumes of interest (VOIs) were delineated using the CT image for guidance. The activity concentrations in the VOIs were compared with the activity concentration estimated from the phantom preparation.

2.2. Monte Carlo simulations

Gamma-camera projections of ^{223}Ra in equilibrium with its daughters were simulated using the SIMIND Monte Carlo program (Ljungberg and Strand 1989). Both MEGP and HEGP collimators were considered and the full collimator model in SIMIND based on Monte Carlo ray-tracing (Ljungberg *et al* 2005) was used. The photon emission spectrum of the decay chain was constructed using a combination of calculated yields for ^{223}Ra in equilibrium with its daughters starting from the values reported by LNHB (www.nucleide.org/DDEP_WG/DDEPdata.htm) (Be *et al* 2010, Be *et al* 2011, Be *et al* 2013) and the yields reported by Pibida *et al* (2015) directly for ^{223}Ra in equilibrium with its daughters. The yields reported by Pibida *et al* were used when available and completed with the calculated yields when necessary.

2.2.1. Validation

The Monte Carlo program was evaluated for simulation of ^{223}Ra using two sets of measurements obtained with the same gamma camera that was used for the phantom measurements. The first measurement was of a syringe filled with 2.2 MBq ^{223}Ra in a volume of 5.4 mL. A planar projection was acquired in a 128 × 128 matrix (pixel size 4.4 × 4.4 mm^2) during 45 min. The second measurement was a planar projection of the phantom used for SPECT acquisitions with sphere 3 filled with an activity of 0.12 MBq in a cold background. The projection time was 30 min, and the pixel size was 4.4 × 4.4 mm^2. Both measurements employed an MEGP collimator.

The measurements were replicated in SIMIND and the profiles compared. It was realized that an important component of the measured profiles was a general background. Because this component could not be included directly in the Monte Carlo simulation, the background count rate was estimated using the blank scan used in the calibration procedure for the phantom measurements. This component was added to the simulated profiles in the comparison.

2.2.2. Spheres

A CT image of the phantom used for physical experiments was converted to densities as described in section 2.1.1. The three spheres were manually delineated, and the resulting masks (in the CT image voxel size) were used as source maps for MC simulations of spheres filled with activity (26.5 mL, 11.5 mL, and 5.4 mL) using the SIMIND Monte Carlo program. A background source compartment was also constructed. The geometry is illustrated in figure 1. Simulations were performed for each sphere and the background

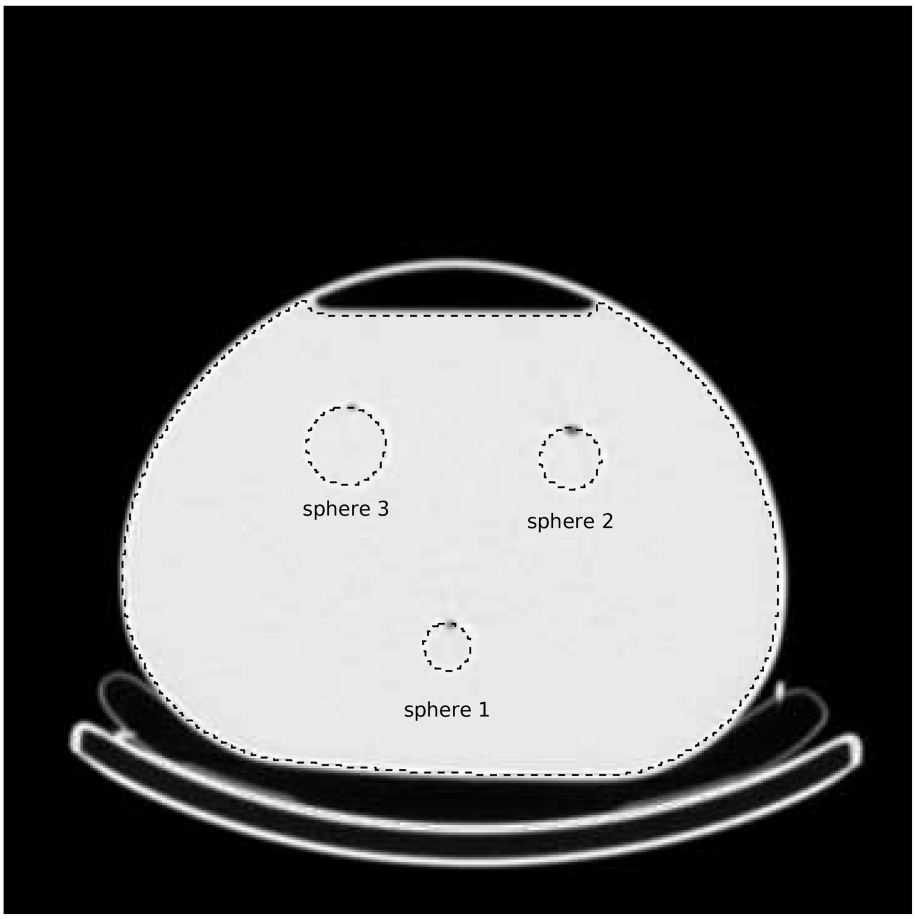

Figure 1. Geometry used for simulation of spheres. The density map is shown in the background, and the boundaries of the source compartments are shown as dashed lines.

compartment separately. The SIMIND Monte Carlo program uses variance reduction techniques to achieve low-noise projections. The simulations are thus run until the residual Monte Carlo noise is negligible, and noise corresponding to the measurement conditions is added in a separate step. Complete projections were constructed by linear combinations of the different projections that were scaled according to the assumed acquisition time and activity in each compartment. Three different scenarios were constructed: A single sphere (sphere 3) with an activity concentration of 4.5 kBq mL^{-1} without background, all three spheres with an activity concentration of 4.5 kBq mL^{-1} without background, and all three spheres with an activity concentration of 1.6 kBq mL^{-1} with background (SBR 20:1). Poisson-distributed noise was added in ten noise realizations per case.

Reconstruction was performed as for the physical phantom measurements. The sensitivity used for calibration of the system was derived through simulation of a thin vertical cylinder of activity in air processed as for the physical phantom measurements. The reconstructed images were interpolated to the CT voxel size, and the activity concentration in the spheres was estimated using the masks used as source maps in the Monte Carlo simulations to construct VOIs and compared with the concentrations defined in the simulations. The means and standard deviations over the noise realizations were computed. In addition, the errors for images reconstructed from noise-free projections were calculated.

2.2.3. Anthropomorphic phantom

A modified male XCAT computer phantom (Segars *et al* 2010) voxelized with a voxel size of $2.21 \times 2.21 \times 2.21$ mm^3 was used as the geometry and source distribution. Three voxelized spheres with volumes of 34 mL, 70 mL, and 100 mL were added to the phantom skeleton in order to simulate lesions. The total activity in the phantom (including arms) was set to 4.2 MBq. The activity concentration in the lesions was varied between 0.5 kBq mL^{-1}, 1 kBq mL^{-1}, 2 kBq mL^{-1} and 4 kBq mL^{-1}. The remaining activity was split equally between the remaining skeleton and the large intestine content. The assumed distribution for normal organs is in line with what has been reported in the literature at 1 d p.i. (Carrasquillo *et al* 2013, Chittenden *et al* 2015, Yoshida *et al* 2016). The range of activity concentrations for lesions was motivated by the studies of Pacilio *et al* (2016*a*) and Murray *et al* (2017), where the absorbed doses and half-lives reported

Table 2. Relative activity concentration deviations (in percentages) for spheres in SPECT images acquired with MEGP and HEGP collimators. Sphere 1 has a volume of 5.5 mL, sphere 2 has a volume of 11.5 mL and sphere 3 has a volume of 26.4 mL. Negative values indicate that a lower activity concentration was estimated in the SPECT images than in the phantom preparation.

Spheres	Activity concentration/(MBq mL^{-1})	SBR	Error 1 (%)	Error 2 (%)	Error 3 (%)
		MEGP collimator			
3	4.5	1:0	–	–	−25
1, 2, 3	4.5	1:0	−69	−37	−33
1, 2, 3	3.4	20:1	−64	−37	−34
1, 2, 3	2.5	20:1	−59	−35	−33
1, 2, 3	1.6	20:1	−65	−47	−28
		HEGP collimator			
1, 2, 3	4.5	1:0	−30	−17	−15
3	3.6	1:0	–	–	−24
1, 2, 3	3.4	20:1	−38	−39	−17
1, 2, 3	2.5	20:1	−20	−38	−30
1, 2, 3	1.6	20:1	−86	−25	−31

would correspond to average concentrations of approximately 1 kBq mL^{-1} for an injected activity of 55 kBq kg^{-1}. Two versions of the phantom were constructed for each activity concentration: One with activity only in the lesions and the other with activity in the background organs too. Poisson-distributed noise was added in ten noise realizations for each case. The source geometry used in the simulation is illustrated in figure 2. Because inclusion of the arms would result in unrealistically large projection distances, the arms were omitted in the simulations, and the activity in different compartments scaled accordingly.

Reconstruction was performed as for the physical phantom measurements. The reconstructed images were interpolated to the same voxel size as the phantom, and the means and standard deviations over the ten noise realizations were computed for the different lesions using the source lesion source masks as the basis for defining VOIs. The means and standard deviations over the noise realizations were computed. In addition, the errors for images reconstructed from noise-free projections were calculated.

2.2.3.1. Recovery coefficients

A series of SPECT acquisitions of spheres of different volumes (range 10 mL to 125 mL) in a non-radioactive background was simulated in a cylindrical phantom (radius 15 cm). The activity concentration was set to 10 kBq mL^{-1} and the time per projection to 2 min. The reconstruction and post-processing (i.e. interpolation to a smaller voxel size to facilitate the analysis) was as for the anthropomorphic phantom. The recovery was determined as a function of volume and a recovery coefficient (RC) curve fitted according to (Gustafsson *et al* 2017, Ilan *et al* 2015)

$$\mathrm{RC}(V) = \frac{1}{1 + \left(\frac{\alpha}{V}\right)^{\beta}}, \tag{1}$$

where V is the volume and α and β are two fitting parameters.

The derived RC curve was used to correct the activity concentrations for the lesions in the anthropomorphic phantom in a separate evaluation.

3. Results

3.1. Phantom measurements

The deviations in activity concentrations estimated in the SPECT images and in the phantom preparation are presented in table 2. All the estimated activity concentrations with SPECT are lower than the reference values estimated in the phantom preparation, especially for the smallest sphere, which is sometimes underestimated by more than 60%. An example of a reconstructed SPECT image for an activity concentration of 4.5 kBq mL^{-1} acquired with an MEGP collimator is shown in figure 3(a) for 8 iterations and 40 iterations.

3.2. Monte Carlo simulations

3.2.1. Validation

Profiles for the syringe and the sphere are shown in figure 4. The leftmost column shows the raw data for the measurements and the simulations scaled to the activities and acquisition time employed in the measurements. In the rightmost column, both measured and simulated profiles have been normalized to a

Figure 2. Source geometry for the simulation of SPECT images of a XCAT phantom. Activity is assigned to the skeleton, the content of the large intestine (green), and to lesions (red).

maximum of 1. For the sphere measurement, the sum of five consecutive rows was used to generate the profiles, to increase the SNR for the measured profiles. The simulations overestimate the maximum value (and sum) of the profiles, but the shapes of the profiles agree when normalized.

3.2.2. Spheres

The relative errors in the activity concentration and associated standard deviations are presented in table 3. The average underestimation increases for small spheres and spheres with a warm background compared to large spheres and spheres with a cold background. The standard deviations are 4% to 7% for the largest sphere (sphere 3) and increase to up to 20% for the smallest sphere.

3.2.3. Anthropomorphic phantom

The activity concentration errors and the associated standard deviations in the different lesions are shown in figure 5, which also indicates the error obtained in SPECT images reconstructed from noise-free projections. The tendency is that the average underestimation decreases with increasing volume, but also with increasing activity concentration. For the smallest lesion (lesion 1) with an MEGP collimator, the average activity-concentration error decreases from −46% to −23% (with background) and −27% to −21% (without background) when the activity concentration increases from 0.5 kBq mL^{-1} to 4 kBq mL^{-1}. The corresponding results for the HEGP collimator are −28% to −18% (with background) and from −23% to −14% (without background). The trends are similar for the other lesions. The concentrations estimated from noise-free projections change less as a function of concentration, with lesion 1 with an MEGP collimator going from −22% to −18% with background and for the case without background being stable at −16%. The corresponding results for HEGP are −18% to −14% and −12%. An example of a reconstructed SPECT image for the case of an MEGP collimator and an activity concentration of 2 kBq mL^{-1} is shown as a maximum-intensity projection in figure 3 (b) for 8 iterations and 40 iterations.

3.2.3.1. Recovery coefficients

The measured recoveries and the fitted recovery curves are shown in figure 6. The results for the estimated activity concentration in the lesions in the phantom are shown in figure 7. The magnitudes of the average errors decrease as compared with the results in figure 5. For the MEGP collimator, the average errors in estimated activity concentration in lesions with the highest concentration are −6%, −3% and −3% (with background) and −4%, 1% and −1% (without background) for lesion 1, 2, and 3, respectively. The corresponding results for HEGP collimator are −7%, 0% and −2% (with background) and −2%, −4% and

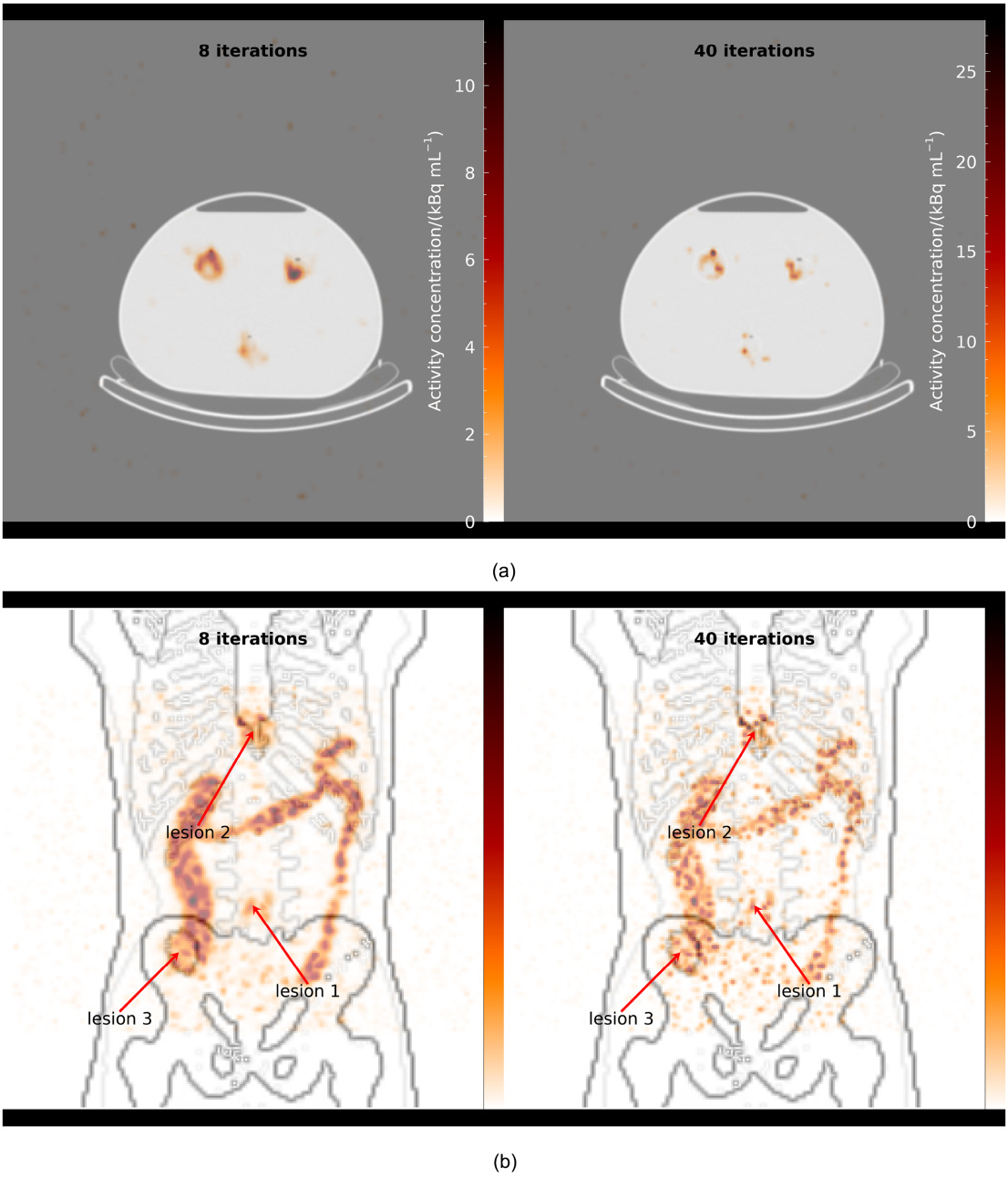

Figure 3. Examples of measured and simulated phantoms for 8 iterations and 40 iterations. (a) shows a slice of the measured phantom with an activity concentration of 4.5 kBq mL^{-1} and no background for the MEGP collimator. (b) shows a maximum intensity projection of a SPECT image for the anthropomorphic phantom with an activity concentration of 2 kBq mL^{-1}. A high-pass-filtered maximum-intensity projection of the density map is shown in the background for anatomical orientation. The different lesions have been marked with arrows. Lesion 3 is partly occulted by the activity in the content of the large intestine.

−1% (without background). However, the trends with respect to the activity concentration remain and the errors are larger for lower activity concentrations.

4. Discussion

This study has investigated the properties of quantitative SPECT for ^{223}Ra by using a series of phantom measurements and Monte Carlo simulations, including simulations in an anthropomorphic phantom. The radionuclide ^{223}Ra is challenging for quantitative imaging, both due its complex emission spectrum and because of the low activities administrated in a typical treatment. The complex emission spectrum, with some photons with an energy of 800 keV having a yield of several percent (Pibida *et al* 2015), makes the application of compensation for penetration and scatter in the collimator important and error prone. Furthermore, the fact that projection data are acquired in an energy window around 82 keV makes it necessary to also include any contribution of characteristic x-rays from lead in the detector model. The low

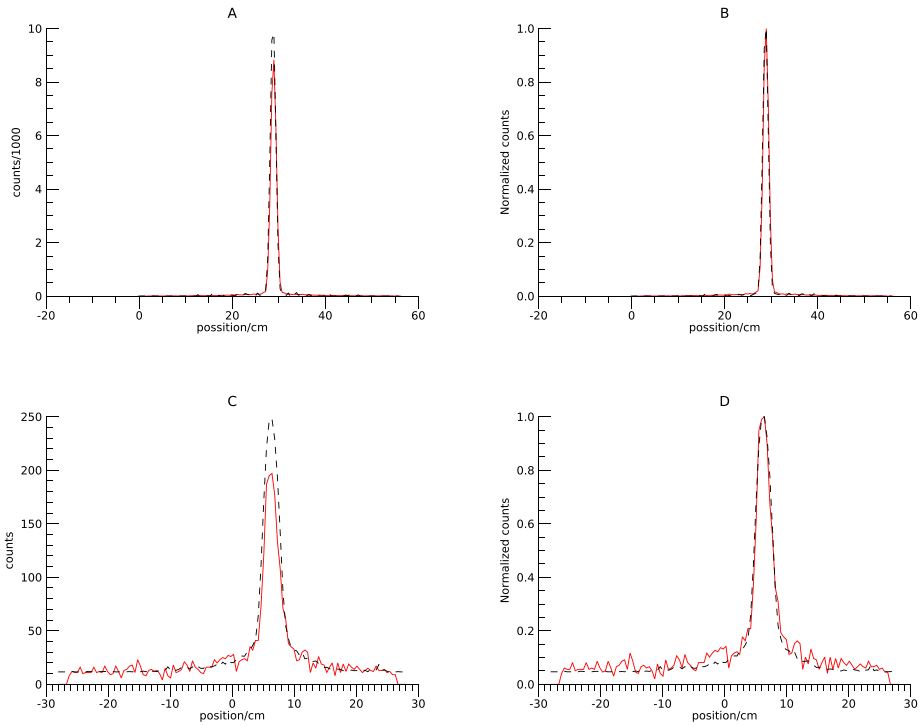

Figure 4. Comparison of measured and simulated profiles for syringe (A and B) and sphere (C and D). Measured profiles are either plotted as is and the simulated profiles scaled according to activity and measurement time (A and C), or the measured profiles and the simulated profiles are normalized to have the same maximum value (B and D).

Table 3. Relative activity concentration deviations (in percentages) for simulated spheres. Negative values indicate that a lower activity concentration was estimated in the SPECT images than in the phantom preparation. Results are presented as the average over the ten noise realizations ±1 standard deviation, and the deviation for the SPECT images reconstructed from noise-free projections is given in parentheses.

Spheres	SBR	Error 1 (%)	Error 2 (%)	Error 3 (%)
		MEGP collimator		
3	1:0	–	–	$-21 \pm 5(-19)$
1, 2, 3	1:0	$-34 \pm 9(-24)$	$-26 \pm 4(-21)$	$-21 \pm 5(-19)$
1, 2, 3	20:1	$-51 \pm 13(-30)$	$-31 \pm 14(-24)$	$-28 \pm 6(-21)$
		HEGP collimator		
3	1:0	–	–	$-16 \pm 7(-15)$
1, 2, 3	1:0	$-22 \pm 9(-22)$	$-21 \pm 6(-19)$	$-17 \pm 4(-16)$
1, 2, 3	20:1	$-44 \pm 20(-30)$	$-31 \pm 12(-22)$	$-23 \pm 6(-18)$

activity involved in the treatment and the resulting poor statistics in the projections is another potential concern, especially considering the ill-conditioned nature of the tomographic-reconstruction problem. Understanding to what extent these factors limit, or even prevent, the utility of SPECT-based activity quantification for ^{223}Ra was the underlying motivation for the study.

There have been few previous studies of clinical quantitative SPECT for ^{223}Ra. The general results from Benabdallah *et al* (2019) and Yue *et al* (2016) are similar to those of the current study, namely that activity quantification with SPECT for ^{223}Ra is feasible, but that there are several problems connected to both deterministic and random effects that need to be handled. As opposed to our study, both those publications employed multiple energy windows rather than the single one at 82 keV employed here, and with respect to Benabdallah *et al* (2019) there are also several methodological differences with respect to, for example, scatter compensation and calibration. The main contribution of our study is that very low activity concentrations, which would be expected to occur in clinical practice, are considered and the insights that are achieved through Monte Carlo simulations, in particular with respect to the repeatability, i.e. the dispersion observed between noise realizations.

The physical phantom measurement shows underestimations in activity concentration of 15% to 34% for the largest sphere (sphere 3) and increasingly larger underestimations for the spheres with lower volumes

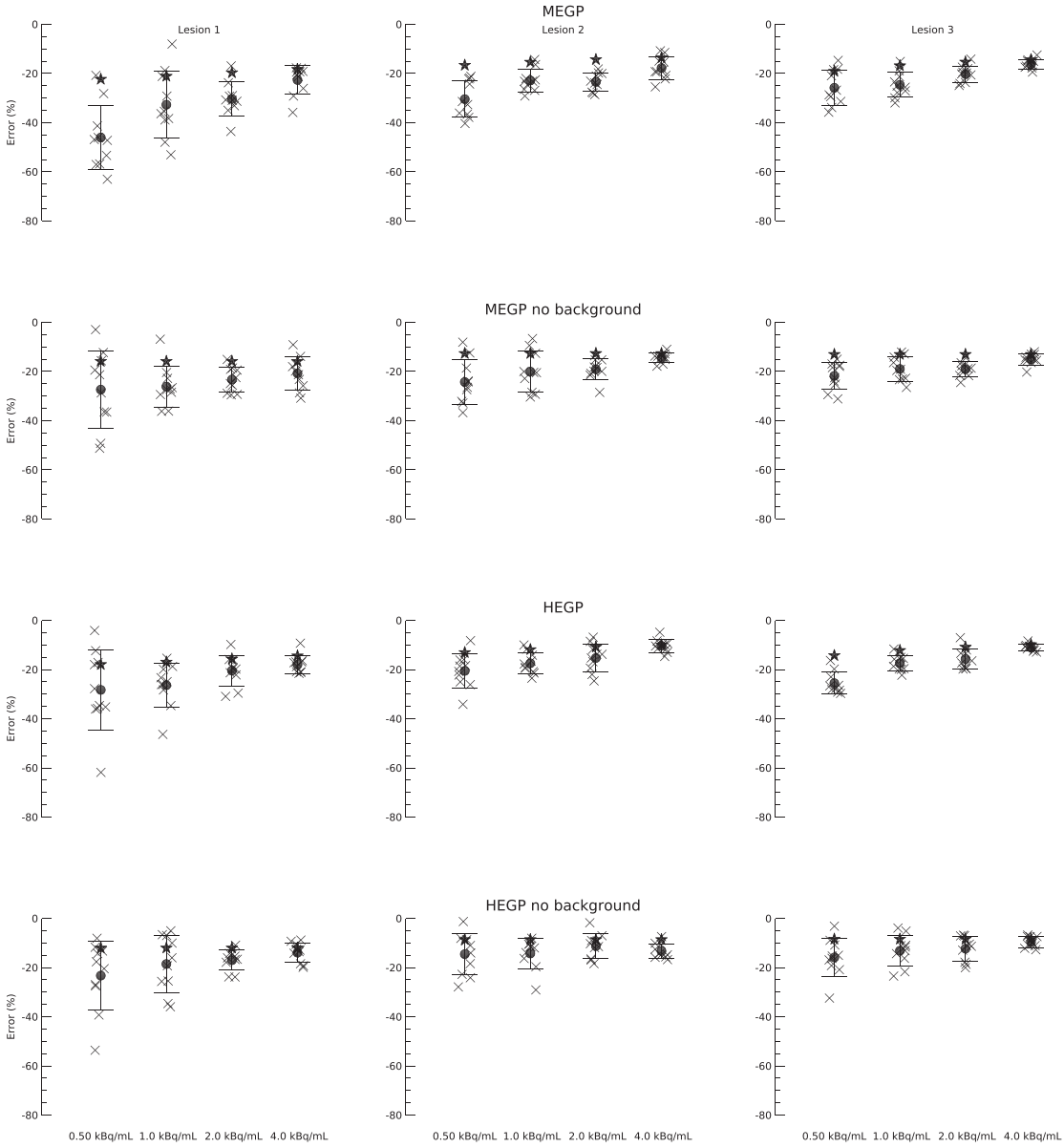

Figure 5. Activity concentration error for the lesions in the XCAT phantoms (lesion 1: 34 mL, lesion 2: 70 mL, lesion 3: 100 mL) for different collimators, and with and without background. The filled circles indicate the mean error over the ten noise realizations, the bars indicate $\pm$ 1 standard deviation, and the filled stars indicate the error in SPECT images obtained from noise-free projections. The crosses show the individual estimated activity concentrations from the SPECT images. The crosses have been randomly moved in the horizontal direction to increase visibility.

(table 2). These deviations are without any post-reconstruction correction for partial-volume effects (e.g. application of recovery coefficients), and an underestimation is thereby to be expected, but the underestimation is larger than is typically observed for the more conventionally used radionuclides (Zeintl *et al* 2010, Gustafsson *et al* 2017). There is also a tendency for the underestimation to be larger than for the simulated counterparts presented in table 3, in particular for the smallest sphere (sphere 1). However, the dispersions over the noise realizations for the simulated spheres are also considerable (from a few percentage points up to 20 percentage points), which should be considered as an indication of the dispersion due to noise that could be expected also for the physical phantom measurements. To some extent, the better estimation for simulated cases can be expected because several aspects are idealized under the simulations compared with the measurements. For example, the VOI definition is ideal, the geometry used in the reconstruction (for attenuation and scatter correction) is identical to the geometry used for the simulation, etc., which should bias the results in favour of the simulations.

The simulations of the anthropomorphic phantom exhibit a similar behaviour as for the physical phantom in the sense that there is a considerable underestimation of the activity concentration and, for the cases of the lower activity concentrations, a considerable dispersion in values obtained over different noise

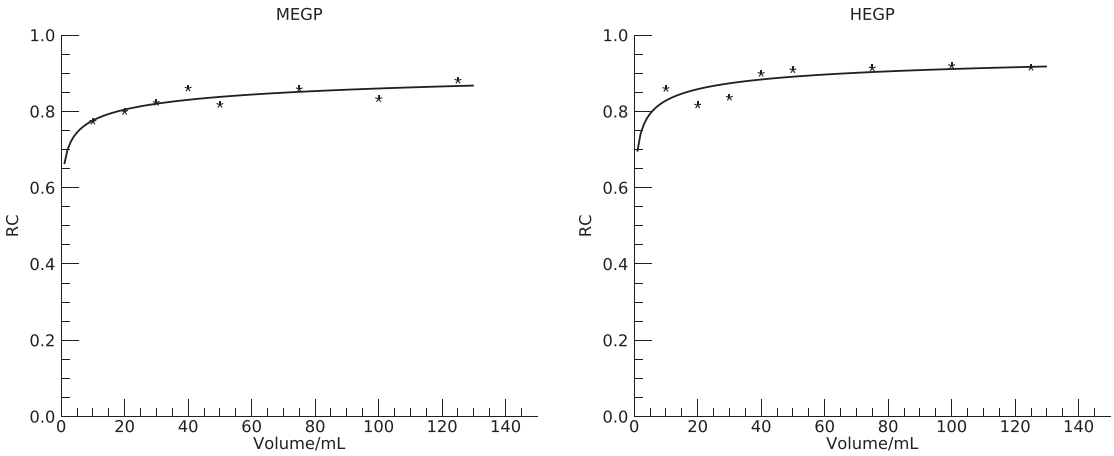

Figure 6. The recovery curves used for spill-out correction, for MEGP (left) and HEGP (right) collimators, respectively.

realizations. There is also a tendency for the average error to decrease (in absolute terms) with increasing activity concentration and for the noise-free projections to result in a lower error than the average error over the ten noise realizations. In theory, the mean of the reconstructed signal is approximately equal to the reconstructed signal of the mean (i.e. noise-free) projections (Barrett *et al* 1994, Wilson *et al* 1994) for ML-EM, but this relationship is known to be approximate and to break down at high noise levels (Van Slambrouck *et al* 2015). The effects of the non-linear properties of the ML-EM algorithms have been observed in previous studies of quantitative SPECT for low count levels (He and Frey 2010). However, for the phantoms with background, part of the increasingly better recovery for increasing activity concentration is also that the object-contrast changes, since the total activity was always kept constant at 4.2 MBq. Accordingly, there is also a decreased error for increasing lesion concentrations for the SPECT images reconstructed from noise-free projections. For the phantoms without background, on the other hand, the change in activity concentration is a simple scaling of the input projections and, as expected, the noise-free projections result in relative errors that do not depend on the underlying concentration. A concentration-dependent bias in the estimated concentration would be difficult to correct for, and hence problematic and further studies of this phenomenon in the context of ^{223}Ra SPECT could be important.

As a way to further study the effect of the low number of counts in the acquired projections, two extra phantom measurements were performed with an extended time of 165 s per projection for an activity concentration of 3.4 kBq mL^{-1} (MEGP collimator) and 2.5 kBq mL^{-1} (HEGP collimator), both with an SBR of 20:1. The resulting relative activity-concentration errors for the MEGP collimator are −50%, −30%, and −33% for spheres 1, 2, and 3, respectively. Hence, the errors are somewhat lower than for the corresponding acquisition with 55 s per projection, but the differences are rather subtle, especially in relation to the fact that that the standard deviations, as projected from the simulation results in table 3, are several percentage points. The corresponding errors for the HEGP collimator are −41%, −34%, and −17%. Unfortunately, we found it very difficult to draw conclusions from these measurements, and the MC simulations turned out to be an easier way to investigate the issue of potential bias for low SNRs.

The lesions (in the form of spheres) studied for the anthropomorphic phantoms have relatively large volumes, all being above 30 mL. This was an active choice in the design of the study, because it was believed that it would not be feasible to quantify small lesions at clinically relevant activity concentrations. The physical phantom measurements with smaller spheres (down to less than 10 mL) also confirmed those assumptions, because the systematic errors and the dispersion of values over different noise realizations would probably not be considered acceptable for patient studies. Post-reconstruction correction of such large discrepancies would risk introducing major uncertainties in the estimated values. As such, the application of ^{223}Ra SPECT to patients would be limited to determining the average concentration in relatively large volumes. In many ways, this situation is similar to the limitations of lesion dosimetry in RNT also for less complex radionuclides, e.g., ^{177}Lu (Roth *et al* 2018), but the size limit is larger and may to some extent depend on total activity also than on volume alone. From a clinical perspective, lesions with lower volumes are likely to also be of interest, but for the two major studies that report absorbed doses to lesions, both report average volumes of similar magnitudes as those studied here, with 28 mL (Murray *et al* 2017) and 114 mL (Pacilio *et al* 2016*a*), respectively.

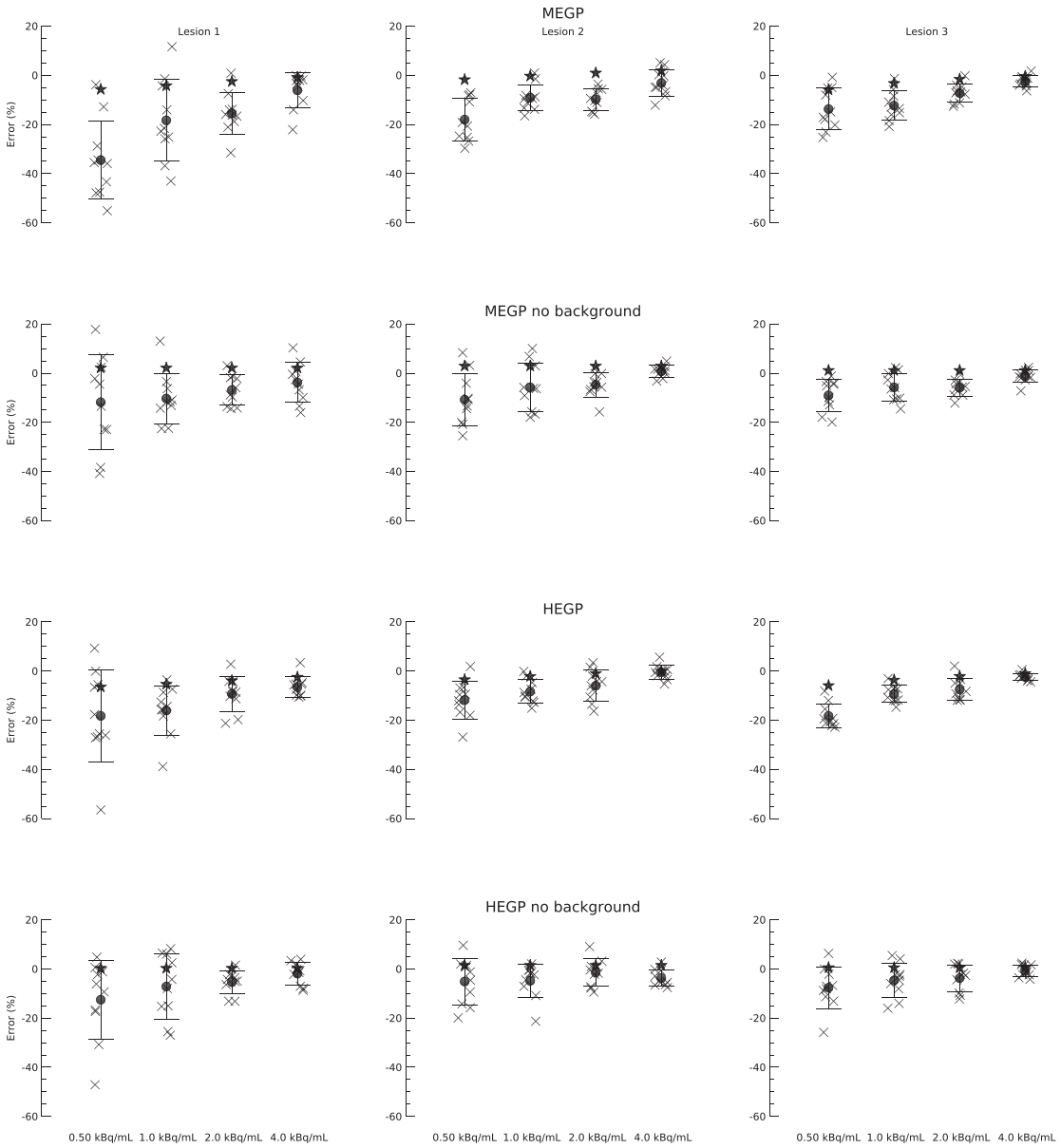

Figure 7. Activity concentration error for the lesions in the XCAT phantoms (lesion 1: 34 mL, lesion 2: 70 mL, lesion 3: 100 mL) for different collimators, and with and without background after application of recovery coefficients according to the curves shown in figure 6. The filled circles indicate the mean error over the ten noise realizations, the bars indicate ± 1 standard deviation, and the filled stars indicate the error in SPECT images obtained from noise-free projections. The crosses show the individual estimated activity concentrations from the SPECT images. The crosses have been randomly moved in the horizontal direction to increase visibility.

The presence of high-energy photons and characteristic x-rays from the collimator makes it necessary to compensate for the whole collimator-detector response; i.e., not only is the blurring effect of imperfect collimation is considered but also the non-static sensitivity as a function of distance from the collimator is modelled in the reconstruction. This complicates the calibration through measurement of the sensitivity in air because the calibration factor would also need to be free from the effects that the reconstruction compensates for. This was handled by normalizing the sensitivity by the total-to-geometric ratio at the source-to-collimator distance used in the calibration measurement. An alternative approach would have been to calibrate the system using a reconstructed SPECT image rather than a planar measurement as discussed by e.g. Zhao *et al* (2018). For example, for the physical phantom the single-sphere measurements could have served as calibration measurements by comparing the total signal in an expanded VOI around the sphere to the total activity in the sphere determined from the phantom preparation. However, estimating total activity for the single-sphere measurements, as determined from the sum in a dilated VOI around the sphere, using the existing calibration from Petri dishes, the errors are −5.8% and −3.1% (in VOIs with volumes of 112 mL) for the MEGP and HEGP collimators, respectively. Hence, such an alternative calibration would not

be fundamentally different from the existing one, and the observed errors with respect to activity concentration for the other spheres in table 2 would change only marginally, especially when considering that the standard deviations presented in table 3 are of the same order as the errors in total activity discussed here. If a similar study of the error in total activity in the lesions for dilated VOIs is performed for the simulated anthropomorphic phantoms without activity in the background, the results are −1.7%, −1.6%, and 3.2% for lesions 1, 2, and 3, respectively, for the SPECT images from noise-free projections acquired with an MEGP collimator. The corresponding values for the HEGP collimator are 4.1%, 3.7%, and 2.7%. Hence, the majority of the observed errors is due to other reasons than the calibration from 'counts' to activity.

The model error in the reconstruction, not reflected in the simulations, can be seen in the comparison between measured and simulated projections in figure 4, where the profiles agree reasonably well in the tails, but the amplitude of the main peak is reduced in the measurement compared with the simulations. One problem that was noted during this study is the reporting of yields for the characteristic x-rays, which are the primary photons in the acquired projections. The growing interest in ^{223}Ra has led to a series of publications that report the yields of the main gamma lines of ^{223}Ra and its daughters (Pibida *et al* 2015, Kossert *et al* 2015, Collins *et al* 2015), but yields for photons below 100 keV were not reported, and older references had to be used. Because these new publications in general report rather substantially different yields compared with older publications, updated values also for characteristic x-rays would have been interesting and could potentially improve the agreement between simulations and measurements. It is also interesting to note that a substantial proportion of the signal is due to the general background, i.e., signal in the gamma camera not originating from any explicit source, that had to be added to the simulated projections in the comparison. This contribution was not included in the SPECT simulation, nor was it included in the reconstruction, which is another possible reason for bias of the simulation results.

There are reasons to believe that the results published herein could be improved by optimization of the acquisition and reconstruction parameters. There has been some discussion in the literature about the relative benefits of different collimators for ^{223}Ra imaging (Takahashi *et al* 2016, Owaki *et al* 2017, Takahashi *et al* 2018). Given the high energy component of the photon emission spectrum of ^{223}Ra, it might be suspected that a high-energy collimator could be superior for quantification since it suppresses hard-to-model effects such as penetration. An illustration of the geometric and non-geometric components for the MEGP and HEGP collimators are shown in figure 8 (a) to (c), which is based on the simulation of a line source (20 cm) and the signal has been decomposed into its geometric and non-geometric (i.e. penetration, scattering in the camera head, and x rays from the collimator) component using the penetrate scoring routine of the SIMIND program (Ljungberg 2012). The plots indicate a slightly higher non-geometric component for the MEGP collimator than for the HEGP collimator. The effect of non-geometric signal can also be seen in the measured projection of the syringe for the MEGP collimator if the grey scale is set with a low upper threshold, as illustrated in figure 8 (d). However, part of that signal is also the general background discussed in the description of the calibration procedure. The Petri dishes used for sensitivity measurement are also shown in figure 8 (d), where the effect of the general background is clearly seen because of the low count rate in these measurements.

Ultimately, the benefits of different collimators for activity estimation should be judged from the accuracy of those estimates. There is a tendency for the HEGP collimator to give lower errors than the MEGP collimator, but the differences are not large compared with the overall errors and the dispersions introduced by noise. This is in line with a slightly lower non-geometric component for the HEGP collimator compared with the MEGP collimator, as demonstrated in figure 8. This simplifies accurate compensation for such effects in the reconstruction, thereby, in theory, giving a slightly improved estimation of activity concentration. However, further characterization would be needed to fully understand how the choice of collimator affects the activity quantification with SPECT for ^{223}Ra.

In terms of reconstruction settings, a large number of iterations was used. A large number of updates is necessary for all structures in the image to converge. At the same time, an increased number of updates is known to amplify noise, which could be considered particularly negative for a low-count application such as ^{223}Ra. The average over the ten noise realizations and the associated standard deviation as a function of the number of iterations is shown in figure 9. The standard deviations are relatively stable as a function of the number of iterations. This demonstrates one aspect of the study, namely, that the evaluation of activity is a strong regularization and the noise properties exhibited with respect to this procedure should not be confused with the noise properties on a voxel level. Hence, we believe that the noise amplification caused by a large number of iterations is outweighed by the decreased influence of partial-volume effects also for such high-noise studies as those investigated in this paper. For the example shown, the average stabilizes after approximately 20 iterations, indicating that a lower number of iterations would have been sufficient. However, it should be noted that the geometry is here relatively simple, and for more complex geometries a higher number of updates is likely to be beneficial (Roth *et al* 2018).

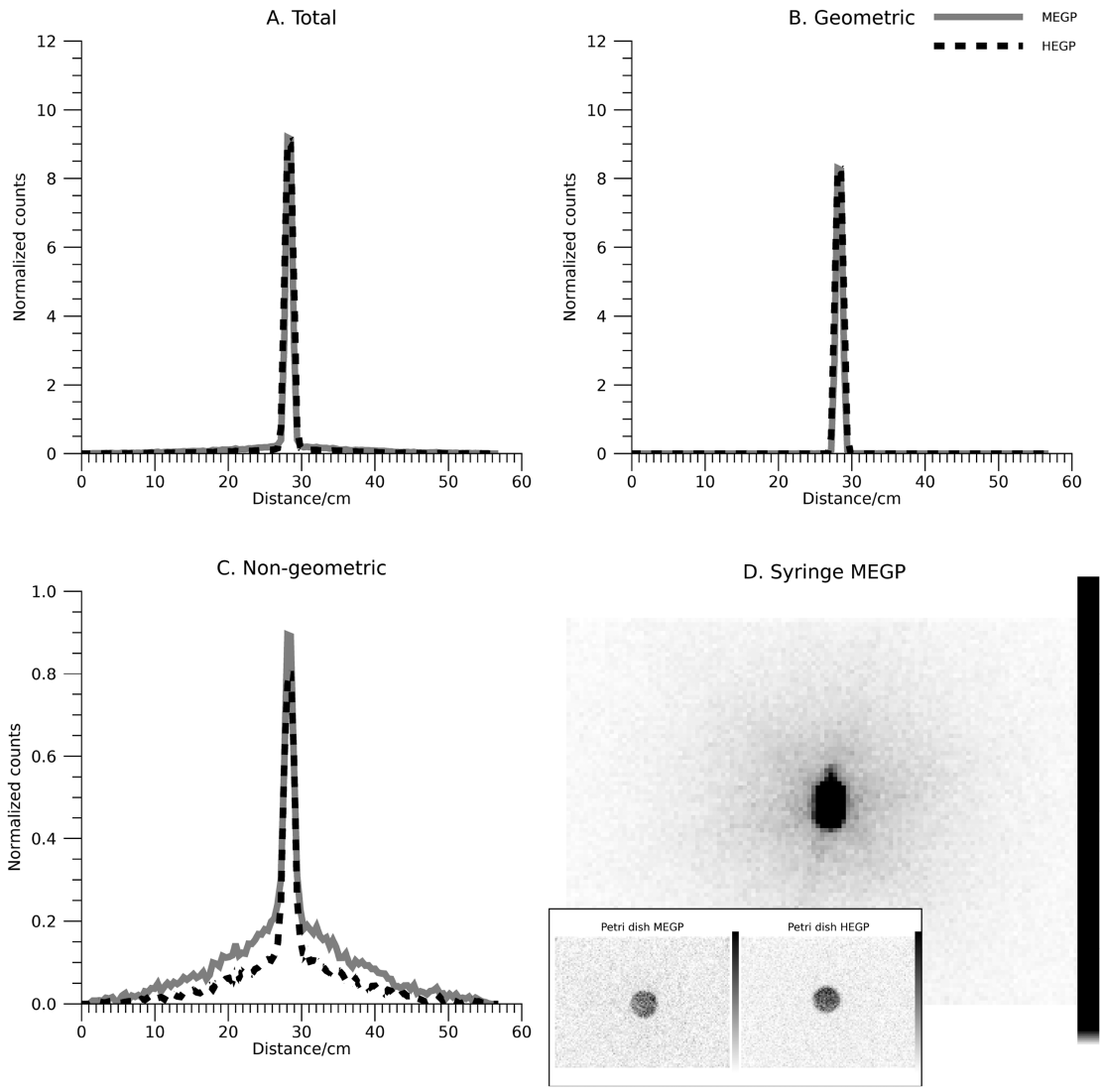

Figure 8. Illustration of geometric and non-geometric components of the the detected signal in the gamma camera for different collimators. Figures (a) to (c) show the profiles (summed over nine consecutive rows) through a simulated line source with the signal decomposed into its geometric and non-geometric components. In this context a geometric photon is a photon that has been detected in the energy window of the crystal by going through a collimator hole without being scattered in the camera head, while the non-geometric component included photons that had penetrated a septum, scattered in the collimator, scattered in the compartment behind the crystal, or was a characteristic x-ray from the the collimator. Note that the range for the ordinate is an order of magnitude lower for the non-geometric component than for the geometric component and total signal. Figure (d) shows measured projections of the syringe used for validation and the Petri dishes sused for calibration of the camera. Note that the grey scale for the syinge image is not linear.

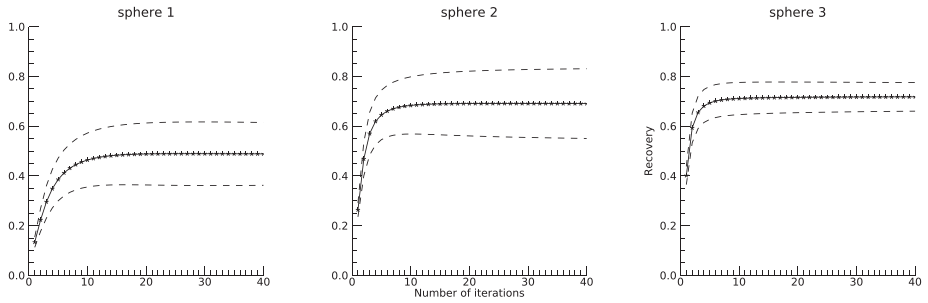

Figure 9. Average recovery and one standard deviation as a function of the number of iterations for the simulated three spheres with background with the MEGP collimator. The number of subsets is 6, so the number of updates is a factor of 6 higher than the number of iterations.

One aspect for image-based estimation of activity concentration is the compensation for partial-volume effects. This aspect has only been partly addressed in the current study. For the anthropomorphic phantom, a

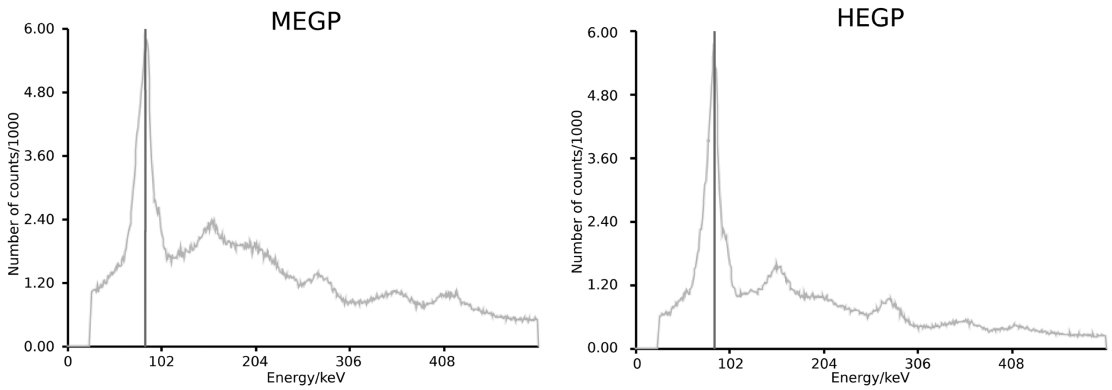

Figure 10. Spectra acquired for a syringe of ^{223}Ra measured with MEGP collimator (left) and HEGP collimator (right). The vertical lines indicate the locations of the main peaks used for acquisition in the current study.

strategy based on the application of RCs was adopted. The effect is a reduction in bias, as seen when comparing figure 5 and figure 7. However, it should be remembered that the use of RCs is, in principle, limited to objects of the same shape as the objects used for deriving the recovery curves, and its application to object with other shapes may result in errors. Hence, the ability of the method to properly account for the spill-out may be somewhat exaggerated in the studied phantom compared to a real-world situation. This is also the main reason why we did not pursue to apply similar corrections for the physical phantom or its simulated counterpart, where the test geometry would, in our minds, be too similar to the geometry used for deriving RCs. The use of RCs is not an ideal way of compensating for partial volume effects, but its simplicity still makes it an attractive method for practical use. However, there are a number of alternative methods available in the literature (Erlandsson *et al* 2012).

One important limitation of the current study is the limited range of volumes considered, and further studies on the effect of volume and activity concentration and their combined effect on the accuracy would be desirable. The fact that only spherical and homogeneous lesions are considered also for the anthropomorphic phantom is another deviation from fully realistic geometries. In principle, simulating non-spherical lesions is easy. The problem is rather the interpretability of the results, which is made more difficult by the application of non-standard shapes.

Another aspect that would deserve attention but that was not considered herein is the application of multiple energy windows to increase the SNR. Considering the high variability of estimates as demonstrated in tables 3 and figure 5, an increased number of collected counts is likely to be beneficial despite the somewhat more complicated reconstruction resulting from the employment of multiple energy windows. Examples of spectra for MEGP and HEGP collimators acquired using a syringe filled with a ^{223}Ra solution are shown in figure 10. Several peaks apart from the combined peaks for characteristic x-rays (around 82 keV) are visible, for example around 150 keV comprised of two gamma emissions from ^{223}Ra at 144 keV and 154 keV, and around 270 keV comprised of one gamma emission from ^{223}Ra at 269 keV and one gamma emission from ^{219}Rn at 271 keV. Such alternative energy spectra have also been used in combination with the characteristic x-rays at 80 keV in some previous studies of ^{223}Ra (Carrasquillo *et al* 2013, Benabdallah *et al* 2019, Pacilio *et al* 2016*a*).

From a metrological point of view, *in vivo* quantification of ^{223}Ra is interesting because of the combination of a complex photon emission spectrum and the low activities resulting in poor image statistics. Hence, better results could be obtained either by improved modelling of the projection-formation process in order to reduce systematic errors or by better handling of the low SNR. With respect to the former, one possible way to improve the model of the projection formation is to use a fully Monte Carlo-based projector (Gustafsson *et al* 2018). The potential of Monte Carlo-based reconstruction for ^{223}Ra has been demonstrated with encouraging results (Sakaguchi *et al* 2018). With respect to the low SNR, the obvious improvement is to include more photo-peaks in the acquisition, as discussed above. However, it could also be of interest to investigate the use of alternative reconstruction algorithms rather than ML-EM or OS-EM that explicitly address the problems associated with low-count tomographic reconstruction (Van Slambrouck *et al* 2015).

5. Conclusions

Activity concentration estimation using SPECT of ^{223}Ra is feasible for reasonably large structures (approximately 30 mL or larger) at concentrations of approximately 1 kBq mL^{-1}. However, poor

repeatability is a major problem that needs to be addressed to improve the reliability of the quantification. There is also a tendency of increased systematic error for decreased activity concentrations.

Acknowledgment

This study was financially supported by Mrs Berta Kamprad's Foundation (FBKS 2017–33). The authors would like to thank Bayer for kindly supplying the radium used for the phantom measurements.

References

Barrett H H, Wilson D W and Tsui B M W 1994 Noise properties of the EM algorithm: I Theory *Phys. Med. Biol* **39** 833–46

Bé M-M, Chisté V, Dulieu C, Mougeot X, Chechev V P, Kondev F G, Nichols A L, Huang X and Wang B 2013 Table of radionuclides vol 7 (Sèvres: Bureau International des Poids et Mesures)

Bé M-M *et al* 2011 Table of radionuclides vol 6 (Sèvres: Bureau International des Poids et Mesures)

Bé M-M *et al* 2010 Table of radionuclides vol 5 (Sèvres: Bureau International des Poids et Mesures)

Benabdallah N, Bernardini M, Bianciardi M, de Labriolle-Vaylet C, Franck D and Desbrée A 2019 ^{223}Ra-dichloride therapy of bone metastasis: optimization of SPECT images for quantification *EJNMMI Research* **9** 20

Carrasquillo J A, *et al* 2013 Phase I pharmacokinetic and biodistribution study with escalating doses of ^{223}Ra-dichloride in men with castration-resistant metastatic prostate cancer *Eur J. Nucl. Med. Mol. Imaging.* **40** 1384–93

Chittenden S J, Hindorf C, Parker C C, Lewington V J, Pratt B E, Johnson B and Flux G D 2015 A phase 1, open-label study of the biodistribution, pharmacokinetics and dosimetry of ^{223}Ra-dichloride in patients with hormone-refractory prostate cancer and skeletal metastases *J. Nucl. Med.* **56** 1304–9

Collins S M, Pearce A K, Regan P H and Keightley J D 2015 Precise measurements of the absolute γ -ray emission probabilities of ^{223}Ra and decay progeny in equilibrium *Appl. Radiat. Isot.* **102** 15–28

Dewaraja Y K, Frey E C, Sgouros G, Brill A B, Roberson P, Zanzonico P B and Ljungberg M 2012 MIRD pamphlet no. 23: Quantitative SPECT for patient-specific 3-dimensional dosimetry in internal radionuclide therapy *J. Nucl. Med.* **53** 1310–25

Erlandsson K, Buvat I, Pretorius P H, Thomas B A and Hutton B F 2012 A review of partial volume correction techniques for emission tomography and their applications in neurology, cardiology and oncology *Phys. Med. Biol.* **57** R119–59

Flux G D 2017 Imaging and dosimetry for radium-223: the potential for personalized treatment *Brit. J. Radiol.* **90** 20160748

Frey E and Tsui B 1996 A new method for modeling the spatially-variant, object-dependent scatter response function *IEEE Nuclear Sci. Symp. Conf. Record* vol **2** (Piscataway, NJ: IEEE) pp 1082–6

Frey E and Tsui B 2005 Collimator-detector response compensation in SPECT *Quantitative Analysis in Nuclear Medicine Imaging* ed Zaidi H (New York: Springer) pp 141–66

Ghaly M, Sgouros G and Frey E 2019 Quantitative dual isotope SPECT imaging of the alpha emitters Th-227 and Ra-223 *J. Nucl. Med.* **60** (suppl. 1) 41

Gustafsson J, Brolin G and Ljungberg M 2018 Monte Carlo-based SPECT reconstruction within the SIMIND framework *Phys. Med. Biol.* **63** 245012

Gustafsson J, Sundlöv A and Sjögreen Gleisner K 2017 SPECT image segmentation for estimation of tumour volume and activity concentration in ^{177} Lu-DOTATATE radionuclide therapy *EJNMMI Research* **7** 18

He B, Du Y, Song X, Segars W P and Frey E C 2005 A Monte Carlo and physical phantom evaluation of quantitative In-111 SPECT *Phys. Med. Biol.* **50** 4169–85

He B and Frey E C 2010 Effects of shortened acquisition time on accuracy and precision of quantitative estimates of organ activity *Med. Phys.* **37** 1807–15

Ilan E, Sandstrom M, Wassberg C, Sundin A, Garske-Roman U, Eriksson B, Granberg D and Lubberink M 2015 Dose response of pancreatic neuroendocrine tumors treated with peptide receptor radionuclide therapy using ^{177} Lu-DOTATATE *J. Nucl. Med.* **56** 177–82

Kossert K, Bokeloh K, Dersch R and Nähle O 2015 Activity determination of ^{227}Ac and ^{223}Ra by means of liquid scintillation counting and determination of nuclear decay data *Appl. Radiat. Isot* **95** 143–52

Ljungberg M 2012 *Monte Carlo Calculations in Nuclear Medicine: Applications in Diagnostic Imaging* eds M Ljungberg, S E Strand and M A King 2 edn (Boca Raton, FL: CRC Press) ch 7 pp 111–27

Ljungberg M, Larsson A and Johansson L 2005 A new collimator simulation in SIMIND based on the delta-scattering technique *IEEE Trans. Nucl. Sci.* **52** 1370–5

Ljungberg M and Strand S E 1989 A Monte Carlo program for the simulation of scintillation camera characteristics *Comput. Methods Programs Biomed.* **29** 257–72

Murray I, Chittenden S J, Denis-Bacelar A M, Hindorf C, Parker C C, Chua S and Flux G D 2017 The potential of ^{223} Ra and ^{18}F-fluoride imaging to predict bone lesion response to treatment with ^{223} Ra-dichloride in castration-resistant prostate cancer *Eur. J. Nucl. Med. Mol. Imaging* **44** 1832–44

Owaki Y, *et al* 2017 Ra-223 SPECT for semi-quantitative analysis in comparison with Tc-99m HMDP SPECT: phantom study and initial clinical experience *EJNMMI Research* **7** 81

Pacilio M *et al* 2016*a* Dosimetry of bone metastases in targeted radionuclide therapy with alpha-emitting ^{223}Ra-dichloride *Eur. J. Nucl. Med. Mol. Imaging* **43** 21–33

Pacilio M *et al* 2016*b* The Italian multicentre dosimetric study for lesion dosimetry in ^{223}Ra therapy of bone metastases: Calibration protocol of gamma cameras and patient eligibility criteria *Physica Med.* **32** 1731–7

Parker C *et al* 2013 Alpha emitter radium-223 and survival in metastatic prostate cancer *N. Engl. J. Med.* **369** 213–23

Pibida L, Zimmerman B, Fitzgerald R, King L, Cessna J T and Bergeron D E 2015 Determination of photon emission probabilities for the main gamma-rays of ^{223}Ra in equilibrium with its progeny *Appl. Radiat. Isot.* **101** 15–19

Roth D, Gustafsson J, Sundlöv A and Sjögreen Gleisner K 2018 A method for tumor dosimetry based on hybrid planar-SPECT/CT images and semiautomatic segmentation *Med. Phys.* **45** 5004–18

Rubini G, Nicoletti A, Rubini D and Asabella A N 2014 Radiometabolic treatment of bone-metastasizing cancer: From ^{186} Rhenium to ^{223} Radium *Cancer Biother. Radiopharm.* **29** 1–11

Sakaguchi K, Yoshida S, Watanabe S, Hanaoka K, Matano K, Okumura M, Hosono M and Ishii K 2018 Evaluation of iterative reconstruction compensated by Monte Carlo simulation for quantitative radium-223 SPECT *Eur. J. Nucl. Med. Mol. Imaging* **45** (Suppl. 1) S122

Segars W P, Sturgeon G, Mendonca S, Grimes J and Tsui B M W 2010 4D XCAT phantom for multimodality imaging research *Med. Phys.* **37** 4902–15

Takahashi A, Baba S and Sasaki M 2018 Assessment of collimators in radium-223 imaging with channelized hotelling observer: a simulation study *Ann. Nucl. Med.* **32** 649–57

Takahashi A, Miwa K, Sasaki M and Baba S 2016 A Monte Carlo study on ^{223}Ra imaging for unsealed radionuclide therapy *Med. Phys.* **43** 2965–74

Van Slambrouck K, Stute S, Comtat C, Sibomana M, van Velden V, Boellaard R and Nuyts J 2015 Bias reduction for low-statistics PET: Maximum likelihood reconstruction with a modified poisson distribution *IEEE Trans. Med. Imag.* **34** 126–36

Wilson D W, Tsui B M W and Barrett H H 1994 Noise properties of the EM algorithm: II. Monte Carlo simulations *Phys. Med. Biol.* **39** 847–71

Yoshida K *et al* 2016 Pharmacokinetics of single dose radium-223 dichloride (BAY 88-8223) in Japanese patients with castration-resistant prostate cancer and bone metastases *Ann. Nucl. Med.* **30** 453–60

Yue J, Hobbs R, Sgouros G and Frey E 2016 Quantitative SPECT imaging of Ra-223 in a phantom *Med. Phys.* **43** 3407 6Part8

Zeintl J, Vija A H, Yahil A, Hornegger J and Kuwert T 2010 Quantitative accuracy of clinical ^{99m}Tc SPECT/CT using ordered-subset expectation maximization with 3-dimensional resolution recovery, attenuation and scatter correction *J. Nucl. Med.* **51** 921–8

Zhao W, Esquinas P L, Hou X, Uribe C F, Gonzalez M, Beauregard J M, Dewaraja Y K and Celler A 2018 Determination of gamma camera calibration factors for quantitation of therapeutic radioisotopes *EJNMMI Physics* **5** 8